

# VORTEX STRUCTURES AND TURBULENT STATISTICS IN TURBULENT FLOW BEHIND AN ORIFICE

Soichiro Makino, Kaoru Iwamoto\* and Hiroshi Kawamura  
 Department of Mechanical Engineering,  
 Tokyo University of Science  
 Noda-shi, Chiba 278-8510, Japan  
 a7502126@rs.noda.tus.ac.jp

\* Present address: Department of Mechanical Systems Engineering,  
 Tokyo University of Agriculture and Technology  
 Koganei-shi, Tokyo 184-8588, Japan.

## ABSTRACT

Direct numerical simulation (DNS, hereafter) of a turbulent channel flow with an orifice has been performed in order to investigate the turbulent statistics and the vortex structures behind the orifice. The Reynolds numbers based on the friction velocity and the channel half width are 10 – 600. In the wake region, the mean flow becomes asymmetric in wall-normal direction by the Coanda effect. Large-scale vortices are generated at the height of the orifice edges. These vortices become deformed in various scenarios and break up into disordered small-scale structures in the shear layers behind the orifice. The small-scale vortices are convected toward the channel center. The contraction effect can be observed just behind the orifice. The turbulent kinetic energy and the Reynolds stresses increase in the free shear layers. In addition, we classify the wake region based upon the budgets of the Reynolds stresses. The several differences are found in the Reynolds stress budgets between in this study and for a backward-facing step turbulence.

## INTRODUCTION

Separation and reattachment of turbulent flows occur in many practical engineering applications. In the numerical studies of separated flows, the flow over a backward-facing step (Le *et al.*, 1997), the ribbed channel (Leonardi *et al.*, 2003) and the roughened channel flow (Nagano *et al.*, 2004) are frequently employed. In particular, the flow through a two-dimensional backward-facing step is the most popular. Le *et al.* (1997) performed DNS of a turbulent flow over a backward-facing step and evaluated several quantities such as the reattachment length, the Reynolds stresses and the turbulent kinetic energy budgets. The effects of step height were studied by Chen *et al.* (2006). The Kelvin-Helmholtz (K-H) vortices and the longitudinal vortices were observed behind the step (Neto *et al.*, 1993).

On the other hand, DNS of a turbulent flow with an orifice has never been performed to the authors' knowledge. The orifice is often used to control and measure the flow rate in mechanical equipments. In this flow, the separation, the reattachment and also the contraction occur near and behind the orifice.

In the present work, DNS of a laminar and a turbulent channel flow with a rectangular orifice has been carried out for  $Re_{\tau 0}(= u_{\tau 0}\delta/\nu) = 10 - 600$ , where  $u_{\tau 0}$  is the friction velocity calculated from the mean pressure gradient imposed

to drive the flow,  $\delta$  the channel half width and  $\nu$  the kinematic viscosity. The purposes of this study are to obtain the turbulent statistics for the development in turbulence modeling and to examine the contraction effect and the vortex structures behind the orifice.

## NUMERICAL PROCEDURES

The configuration of the computational domain is shown in Fig. 1. The periodic boundary conditions are employed in the streamwise ( $x$ ) and spanwise ( $z$ ) directions. We also tested a inlet-outlet boundary condition case with the driver section (not shown here). The differences of the mean velocities and the fundamental turbulent statistics behind the orifice are within 10 % between for the periodic and for the inlet-outlet case at the same bulk Reynolds number. This is because the streamwise domain length is assigned so long in the periodic case. The no-slip boundary conditions are used on all the walls. The direct forcing immersed boundary method (Fadlum *et al.*, 2000) is applied on and inside the orifice. The flow is driven by the mean pressure gradient.

The governing equations are the incompressible continuity and Navier-Stokes equations:

$$\frac{\partial u_i^+}{\partial x_i^*} = 0, \quad (1)$$

$$\frac{\partial u_i^+}{\partial t^*} + u_j^+ \frac{\partial u_i^+}{\partial x_j^*} = -\frac{\partial p^+}{\partial x_i^*} + \frac{1}{Re_{\tau 0}} \frac{\partial^2 u_i^+}{\partial x_j^{*2} \partial x_j^{*2}} + F_i^+, \quad (2)$$

where  $u$  and  $p$  denote velocity vector and pressure, respectively. The quantities with superscript of + indicate those normalized by  $u_{\tau 0}$  and with superscript of \* are normalized by  $\delta$ . The additional  $F_i^+$  in eq. (2) is the body force term for the immersed boundary method. It can be assume the expression

$$F_i^+ = -RHS_i^+ + \frac{\tilde{u}_i^+ - u_i^{n+}}{\Delta t^*}, \quad (3)$$

where RHS contains the convective, the viscous and the pressure gradient terms in eq. (2) and  $\tilde{u}_i^+$  is the predictor.

The SMAC (Simplified Marker and Cell) method is adopted for the coupling between the continuity and the Navier-Stokes equations. The 2nd-order Crank-Nicolson scheme and the compact-storage 3rd-order Runge-Kutta scheme are employed as the time-advance algorithm: the former for the vertical viscous term, the later for the other viscous and the convection terms. The finite difference

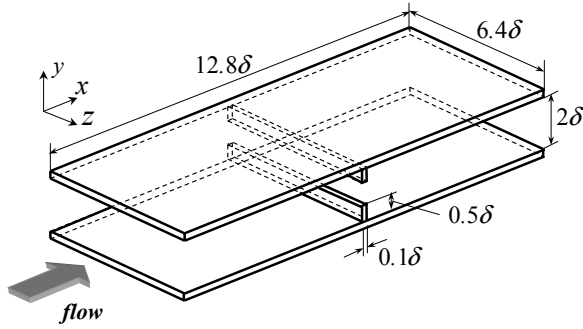


Figure 1: Configuration of the computational domain.

Table 1: Computational Condition.

	10 ~ 20 (4cases)	30 ~ 600 (9cases)
$Re_{\tau_0} (= u_{\tau_0} \cdot \delta / \nu)$	10 ~ 20 (4cases)	30 ~ 600 (9cases)
$Re_b (= u_b \cdot 2\delta / \nu)$	40 ~ 112	180 ~ 3000
$\beta$		0.5
Computational volume	12.8δ × 2δ × 6.4δ	
Grid number	128 × 96 × 64	512 × 128 × 256
Spatial Resolution ( $\Delta x^+$ )	2.00	3.84
Spatial Resolution ( $\Delta y^+$ )	0.039 ~ 0.825	0.235 ~ 5.29
Spatial Resolution ( $\Delta z^+$ )	2.00	3.84
Total statistical time ( $T^+$ )	10000	

method is used for the spatial discretization: the 2nd-order central scheme is employed in all the directions.

The computational conditions are summarized in Table 1. The ratio of slit height of the orifice to channel height  $\beta$  is set to be 0.5, i.e., the distance between the wall and orifice edge  $h$  is  $0.5\delta$  in this study. The spatial resolutions for the lower Reynolds numbers of  $Re_{\tau_0} = 10 - 20$  are the values in the case of  $Re_{\tau_0} = 20$  and the values for the higher cases of  $Re_{\tau_0} = 30 - 600$  are those in  $Re_{\tau_0} = 600$ . These spatial resolutions are calculated from the streamwise-averaged friction velocity.

## RESULTS AND DISCUSSION

### Asymmetry phenomena and mean reattachment length

The streamlines of the mean flow for  $Re_{\tau_0} = 600$  are given in Fig. 2. The mean flow is asymmetry behind the orifice, which is similar to the flow in a sudden expansion (Fearn *et al.*, 1990). These phenomena are referred to as the Coanda effect. The asymmetry direction, the upper or lower, depends on the initial flow field.

A large primary bubble is observed from the back-end of the orifice to  $9\delta$  in the  $x$ -direction at the lower wall ( $L_{r1}$  in Fig. 2). In addition, a secondary bubble (B in Fig. 2) generates to approximately  $7.3\delta$  in the  $x$ -direction (see  $L_{r2}$  in Fig. 2), i.e.,  $1.8h$  from the orifice. Le *et al.* (1997) reported that the length of the secondary bubble in the  $x$ -direction  $L_{r2}$  is  $1.76h$  in a backward-facing step, where  $h$  is the height of the back step. Therefore, the length of the secondary bubble is almost same in both the cases.

The reattachment length  $L_{r1}$  and the secondary bubble length  $L_{r2}$  are shown in Fig. 3 as a function of the bulk Reynolds number. In this study, the reattachment location is determined by the location of  $\partial u / \partial y = 0$  at the wall. The length  $L_{r1}$  is defined as the distance from the back-end of the orifice to the reattachment location. Because the mean flow is asymmetry, the  $L_{r1}$  and the  $L_{r2}$  are obtained as an average of those on the upper and lower walls. In the range of  $Re_b < 400$ , the  $L_{r1}$  increases with increasing the Reynolds number. On the other hand, in  $Re_b > 400$

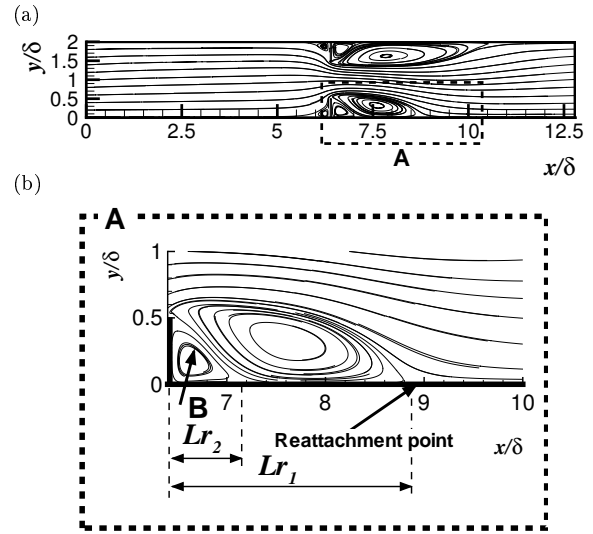


Figure 2: Averaged streamlines for  $Re_{\tau_0} = 600$ . (a) Visualization area is the total computational volume; (b) enlarged view of the rectangular region A in (a).

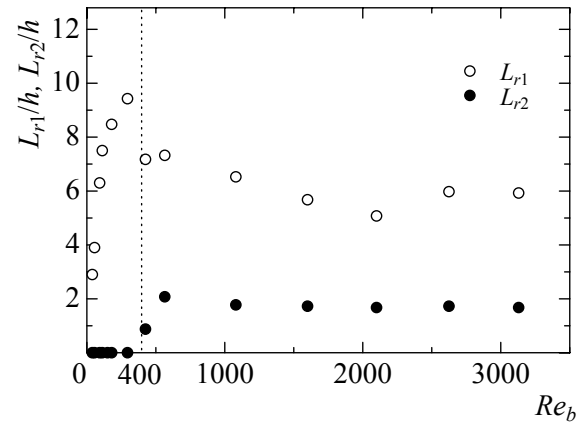


Figure 3: Reynolds number dependence of reattachment length  $L_{r1}/\delta$  and secondary bubble length  $L_{r2}/\delta$  from the back-end of the orifice.

range, the reattachment length  $L_{r1}$  is characterized first by a sharp decrease and subsequently by a gradual one. These results are similar to those described in the case of the backward-facing step experiment (Armaly *et al.*, 1983). One can clearly identify the laminar ( $Re_b < 400$ ), the transitional and the turbulent ( $400 < Re_b < 3300$ ) ranges as implied by the shape of this profile.

The secondary bubble cannot be observed in the laminar region ( $Re_b < 400$ ). In the range of  $400 < Re_b < 550$ , the secondary bubble length  $L_{r2}$  increases with increasing the Reynolds number and it becomes almost constant in  $Re_b > 550$  range. Therefore, the secondary bubble is generated in the transitional and the turbulent regime. In addition, the reattachment length  $L_{r1}$  at a higher Reynolds number ( $Re_b > 2000$ ) is approximately  $6h (= 3\delta)$  in this study. This corresponds roughly to the well-known length of  $5 - 8h$  in the case of the turbulent flow over a backward-facing step (Lesieur, 1997).

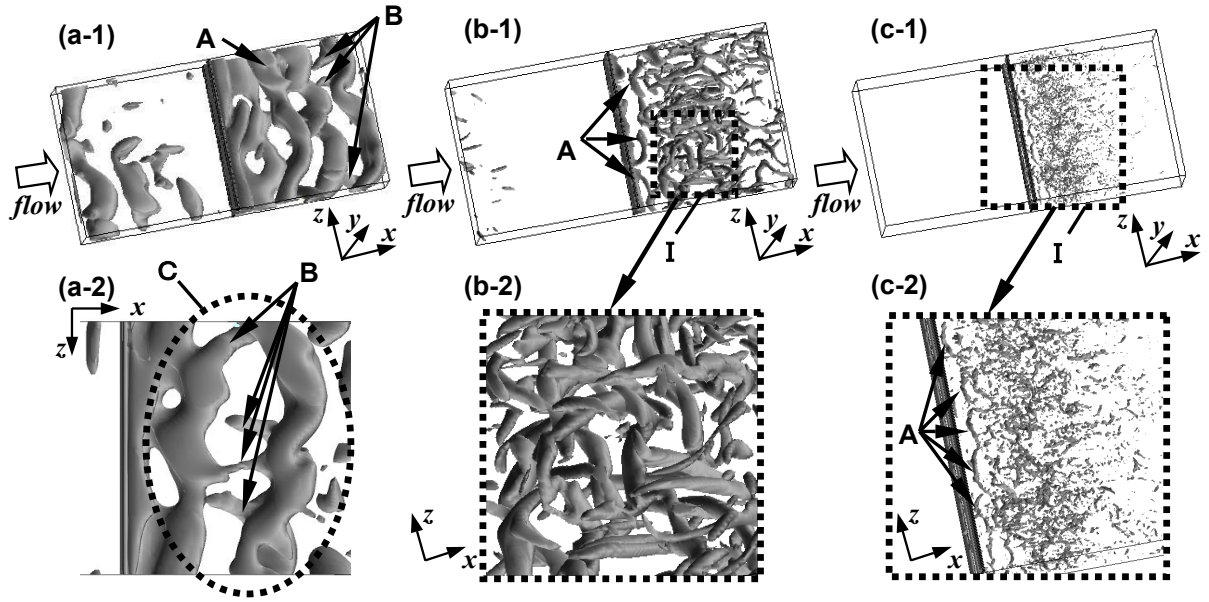


Figure 4: Iso-surfaces of the second invariant of the velocity-gradient tensor  $II^+$ . (a-1)  $II^+ \leq -0.01$  for  $Re_{\tau_0} = 30$ ; (a-2) bottom view of the wake region in (a-1); (b-1)  $II^+ \leq -0.025$  for  $Re_{\tau_0} = 100$ ; (b-2) enlarged view of the rectangular region I in (b-1); (c-1)  $II^+ \leq -0.014$  for  $Re_{\tau_0} = 600$ ; (c-2) enlarged view of the rectangular region I in (c-1).

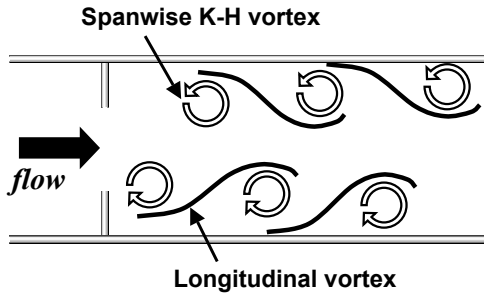


Figure 5: Schematic representation of the vortex structures in the wake region.

#### Vortex structures behind the orifice

The vortex structures for  $Re_{\tau_0} = 30, 100$  and  $600$  are shown in Fig. 4. The vortices are identified by the iso-surface of the second invariant of the velocity-gradient tensor. The spanwise primary K-H vortices are visible in the shear layers behind the orifice (A in Figs. 4(a-1)(b-1)(c-2)). These K-H vortices develop in different ways for different Reynolds numbers.

In the case of  $Re_{\tau_0} = 30$ , they are distorted in the  $z$ -direction and longitudinal vortices are observed between them (B in Figs. 4(a-1)(a-2)). A schematic view of these vortices is shown in Fig. 5. The longitudinal vortices connect one spanwise K-H vortex with another one (C in Fig. 4(a-2)). This three-dimensional vortex structure resembles helical-pairing structure in a mixing layer (Comte *et al.*, 1992) or in a backward-facing step flow (Neto *et al.*, 1993).

For  $Re_{\tau_0} = 100$ , the K-H vortices become deformed more significantly in the  $z$ -direction and break up into disordered small-scale structures. Figure 4(b-2) shows the complex three-dimensional vortex structure with a lattice pattern. The similar vortex pattern is observed in a temporal mixing layer (Comte *et al.*, 1992). The pattern is more complex in the present case. This is mainly due to the effects of the wall

. Neto *et al.* (1993) pointed out in their simulation of the backward-facing step turbulence that a distortion due to the wall was more enhanced for a lower step height than for a higher one.

In the case of  $Re_{\tau_0} = 600$ , the smaller structures are shown in Figs. 4(c-1) and (c-2). The spanwise distorted K-H vortices are observed. The pairing or the lattice structure discussed above, however, is not clearly found because the three-dimensional perturbation increases more significantly.

#### Turbulent statistics behind the orifice

In this section, the turbulent statistics in the case of  $Re_{\tau_0} = 600$  are reported. In Fig. 6, the wake region is classified based upon the budgets of the Reynolds stresses in this study. The transport equation of the Reynolds stresses is expressed as

$$\frac{\partial \overline{u_i'^+ u_j'^+}}{\partial t} = P_{ij} + T_{ij} + D_{ij} + \Pi_{ij} + \phi_{ij} + \epsilon_{ij} + C_{ij}, \quad (4)$$

Production term:

$$P_{ij} = -\overline{u_j'^+ u_k'^+} \frac{\partial U_i^+}{\partial x_k^+} - \overline{u_i'^+ u_k'^+} \frac{\partial U_j^+}{\partial x_k^+}, \quad (5)$$

Turbulent diffusion term:

$$T_{ij} = -\frac{\partial}{\partial x_k^+} \overline{u_i'^+ u_j'^+ u_k'^+}, \quad (6)$$

Molecular diffusion term:

$$D_{ij} = \nu \frac{\partial^2}{\partial x_k^{+2}} \overline{u_i'^+ u_j'^+}, \quad (7)$$

Pressure diffusion term:

$$\Pi_{ij} = -\left( \frac{\partial}{\partial x_i^+} \overline{u_j'^+ p'^+} + \frac{\partial}{\partial x_j^+} \overline{u_i'^+ p'^+} \right), \quad (8)$$

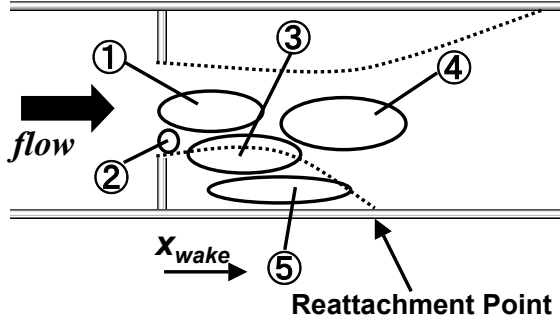


Figure 6: Classification of the wake region for  $Re_{\tau 0} = 600$ .

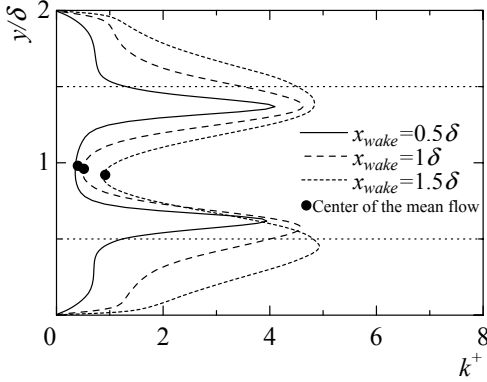


Figure 7: Turbulent kinetic energy profiles for  $Re_{\tau 0} = 600$ .

Pressure strain term:

$$\phi_{ij} = p'^+ \frac{\partial u_j'^+}{\partial x_i^+} + p'^+ \frac{\partial u_i'^+}{\partial x_j^+}, \quad (9)$$

Dissipation term:

$$\epsilon_{ij} = -2\nu \left( \frac{\partial u_i'^+}{\partial x_k^+} \right) \left( \frac{\partial u_j'^+}{\partial x_k^+} \right). \quad (10)$$

The region ① is the channel center near the orifice. The Reynolds stresses and the turbulent kinetic energy in this region are much smaller than in other regions as seen in Fig. 7, where  $x_{wake}$  the streamwise distance from the back-end of the orifice. The minimum value near the channel center is about 8.7 % of the maximum value in the shear layer at  $x_{wake} = 0.5\delta$ . Besides, no evident vortices are observed in this region. Consequently, the flow is close to the potential flow. These potential region is generated by the flow acceleration.

The region ② occupies the shear layer just behind the orifice. The production and convection terms in the budget of  $\overline{u'u'}$  at  $x_{wake} = 0$  are shown in Fig. 8(a), where  $u'$  is the velocity fluctuation in the streamwise direction. Other terms are neglected because their peaks are less than 20 % of the peak value of the production. The production term balances with the convection. These terms exhibit maxima at the same point in the shear layer. Figure 8(b) shows the production terms of  $\overline{u'u'}$  and  $\overline{u'v'}$  for  $0.5 < y/\delta < 0.7$  at  $x_{wake} = 0$ , where  $v'$  indicates the velocity fluctuation in the wall-normal direction. The  $\overline{u'v'}$  production has the peak in the shear layer as the production term of  $\overline{u'u'}$  does. The peak of the  $\overline{u'u'}$  production is caused by the negative mean

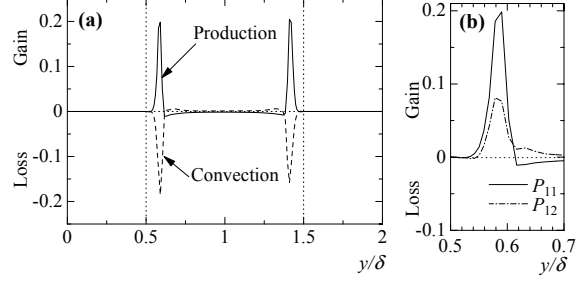


Figure 8: (a) Production term and convection term in the budget of  $\overline{u'u'}$  at  $x_{wake} = 0$  for  $Re_{\tau 0} = 600$ ; (b) production terms in the budgets of  $\overline{u'u'}$  and  $\overline{u'v'}$  at  $x_{wake} = 0$  for  $Re_{\tau 0} = 600$ .

velocity gradient  $\partial U/\partial x$  as shown in Fig. 9 and the peak of the Reynolds stress  $\overline{u'u'}$  in Fig. 10 at the same region. Here,  $U$  and  $V$  are the mean velocities in the streamwise and wall-normal directions, respectively. On the other hand, the peak of the  $\overline{u'v'}$  production is mainly due to the negative  $\partial V/\partial x$  and the increase in the  $u'u'$  as seen in Figs. 9 and 10. Therefore, this positive production of the  $\overline{u'v'}$  is caused by re-spread effect after the contraction. The production term of  $\overline{u'u'}$  also becomes negative near  $y/\delta \approx 0.6$  and  $1.4$  in Figs. 8(a) and (b) ((b) is on the lower side). This is due to the combinations of the positive Reynolds stress  $\overline{u'u'}$  and the positive velocity gradient  $\partial U/\partial x$ , the negative  $\overline{u'v'}$  and the negative  $\partial U/\partial y$  in this region as seen in Figs. 9 and 10. The positive  $\partial U/\partial x$  is caused by the flow acceleration and the negative  $\partial U/\partial y$  by the contraction. The  $\overline{u'v'}$ , moreover, becomes positive for  $0.55 < y/\delta < 0.6$ . The negative  $-\overline{u'v'}$  (i.e., the positive  $u'v'$ ) can be observed near the back-end edge of the roughness elements (Ashrafian *et al.*, 2004). Thus, these positive  $\overline{u'v'}$  are the general tendencies of the flow contraction.

The region ③ indicates the shear layer in the recirculation region. Figure 11 shows the terms in the budget of  $\overline{u'u'}$  at  $x_{wake} = 0.5\delta$ , where the dissipation, the molecular diffusion and the pressure diffusion are not shown for the simplicity. These profiles are characterized by the sharp peaks of the production and the large negative pressure strain for  $0.5 < y/\delta < 0.75$  on the lower side. The mean velocity gradient profiles at  $x_{wake} = 0.5\delta$  are shown in Fig. 12. The peak production of  $\overline{u'u'}$  in Fig. 11 is caused by the large positive mean velocity gradient  $\partial U/\partial y$  as seen in Fig. 12. In the budgets of  $\overline{u'v'}$ , the  $\partial U/\partial y$  mainly contributes to the negative peak of the production term, too (not shown here). Figure 13 displays the budget terms of  $\overline{v'v'}$  at  $x_{wake} = 0.5\delta$ . In the shear layer, the pressure strain term exhibits a large positive value. The similar profiles can be also observed in the budgets of  $\overline{w'w'}$  at  $x_{wake} = 0.5\delta$  (not shown here), where  $w'$  is the velocity fluctuation in the spanwise direction. Hence, the redistribution from  $\overline{u'u'}$  to  $\overline{v'v'}$  and  $\overline{w'w'}$  is the dominant process in this region. It is worth noting that the budgets of the Reynolds stresses and the turbulent kinetic energy in this region are similar to those of a backward-facing step flow (Le *et al.*, 1997) and a plane mixing layer (Rogers *et al.*, 1993). Therefore, the contraction and the existence of the walls add less effects on basic structures in this shear layer.

In the region ④, the turbulent diffusion term is dominant as shown in Fig. 14. This term removes the turbulent energy from the shear layers for  $0.2 < y/\delta < 0.5$  on the lower side and transports it to the channel center where few fluctuations are generated near the orifice. Thus, the turbulent

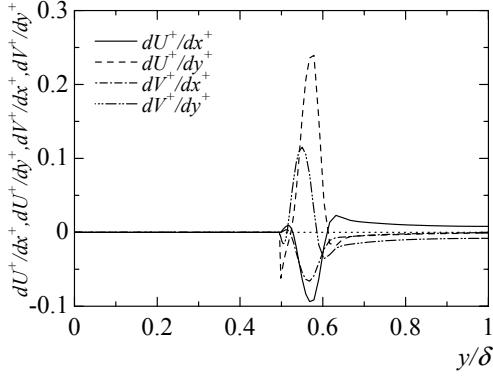


Figure 9: Mean velocity gradient profiles at  $x_{wake} = 0$  for  $Re_{\tau 0} = 600$ .

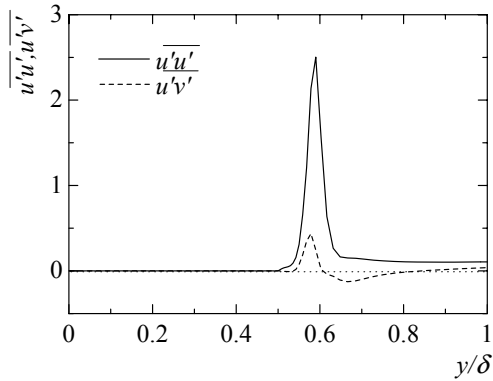


Figure 10: Reynolds stress profiles at  $x_{wake} = 0$  for  $Re_{\tau 0} = 600$ .

diffusion contributes to the increase of the Reynolds stresses and the turbulent kinetic energy in the central region (see in Fig. 7). On the other hand, Le *et al.* (1997) has reported that the turbulent diffusion term transfers the turbulent energy to the near wall region in their backward-facing step simulation. In the present study, two shear layers are generated. Therefore, the turbulent diffusion adds more effects on the turbulent statistics at the channel center than in the backward-facing step flow.

The region ⑤ is located near the wall in the upstream of the reattachment point. Figure 15 shows the terms in the budget of  $\overline{u'u'}$  at  $x_{wake} = 2\delta$  near the wall. The convection term can be neglected. The production term becomes negative owing to the mean reverse flow in the recirculation region. At  $x_{wake} = 2.5\delta$  near the reattachment location on the lower wall (cf. the averaged reattachment length  $L_{r1} \simeq 2.6\delta$  on the lower side), the pressure strain  $\phi_{uu}$  is positive and attains approximately 50 % of the  $\phi_{ww}$  as shown in Fig. 16. This is much larger than that in turbulent plane channel flows. This is because of the splatting effect owing to the flow reattachment.

## CONCLUSIONS

In the present study, we performed DNS of turbulent channel flow with an orifice in various Reynolds numbers and investigated the reattachment location, vortex structures and turbulent statistics.

The Reynolds number dependence of reattachment length corresponds to those described in the case of the backward-facing step experiment. The sharp decrease in the reattachment length can be observed at  $Re_b \simeq 400$ . This region is

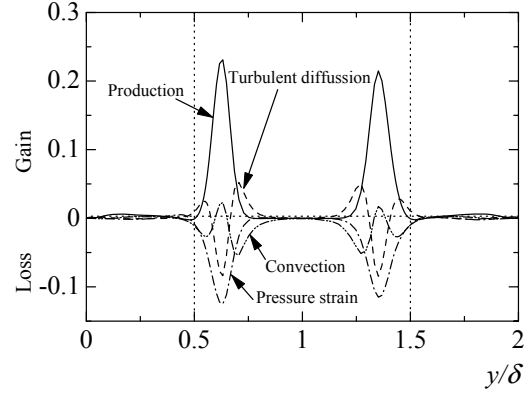


Figure 11: Terms in the budget of  $\overline{u'u'}$  at  $x_{wake} = 0.5\delta$  for  $Re_{\tau 0} = 600$ .

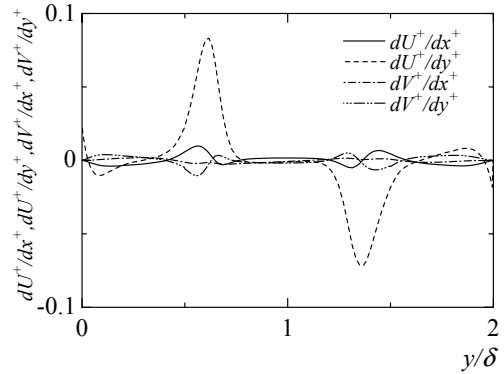


Figure 12: Mean velocity gradient profiles at  $x_{wake} = 0.5\delta$  for  $Re_{\tau 0} = 600$ .

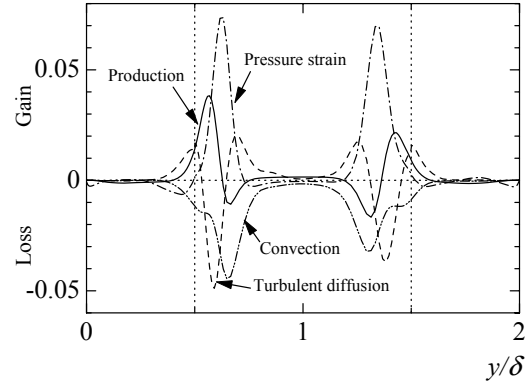


Figure 13: Terms in the budget of  $\overline{v'v'}$  at  $x_{wake} = 0.5\delta$  for  $Re_{\tau 0} = 600$ .

'transition region'. The secondary bubble can be observed in the transitional and the turbulent regime. The length, however, become constant in higher Reynolds number range.

The large-scale K-H vortices are generated just behind the orifice. In lower Reynolds number, the structure like 'helical-pairing structure' in a mixing layer can be observed. This structure becomes more complex with increasing the Reynolds number. The complex three-dimensional vortex structure with a lattice pattern is generated in higher Reynolds number regime. This generation - deformation - breaking up scenario resembles that in the case of turbulent mixing layer and backward-facing step turbulence.

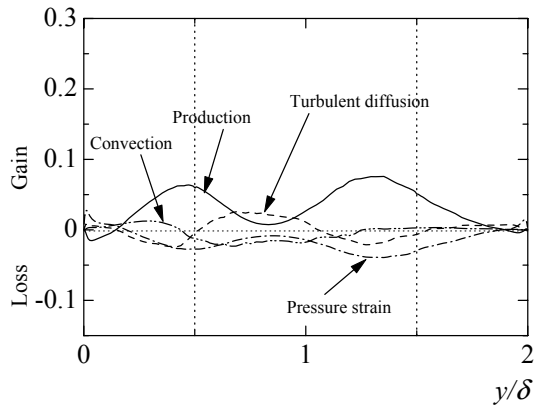


Figure 14: Terms in the budget of  $\overline{u'u'}$  at  $x_{wake} = 2\delta$  for  $Re_{\tau_0} = 600$ .

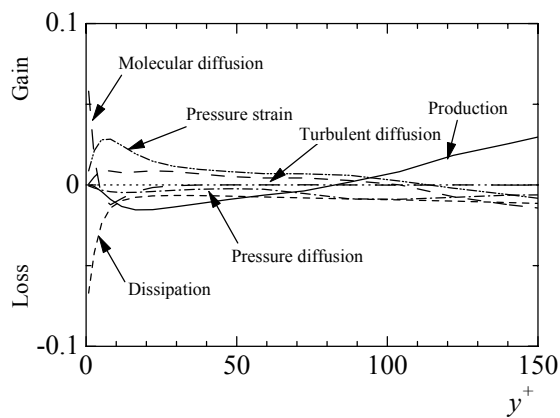


Figure 15: Terms in the budget of  $\overline{u'u'}$  at  $x_{wake} = 2\delta$  near the wall for  $Re_{\tau_0} = 600$ .

The budgets of the turbulent kinetic energy and Reynolds stresses were calculated. We classified the wake region into 5 regions based upon the budgets of the Reynolds stresses. The several differences are found in the Reynolds stresses budgets between in the present case and for a backward-facing step turbulence. The potential region is generated in the channel center near the orifice. In the shear layers just behind the orifice, the Reynolds shear stress  $\overline{u'v'}$  becomes negative because of the contraction effect. In the same region, the positive production term of  $\overline{u'v'}$  is caused by the re-spread effect. In addition, the production term of  $\overline{u'u'}$  exhibits negative value near the orifice edge. This is because of the acceleration and the contraction effects. These behaviors cannot be observed in the backward-facing step turbulence. At the shear layer in recirculation region, the redistribution from  $\overline{u'u'}$  to  $\overline{v'v'}$  and  $\overline{w'w'}$  is the dominant process. At the channel center in the recirculation region, the turbulent diffusion term transfers the turbulent energy from the shear layer to the channel center. In the wall vicinity of the recirculation region, the redistribution from  $\overline{v'v'}$  to  $\overline{u'u'}$  is promoted by the splatting effect.

## REFERENCES

- Armaly, B. F., Durst, F., Pereira, J. C. F. and Schonung, B., 1983, "Experimental and theoretical investigation of backward-facing step flow", *J. Fluids Mech.*, Vol.127, pp. 473-496.
- Ashrafiyan, A., Andersson, H. I. and Manhart, M., 2004,

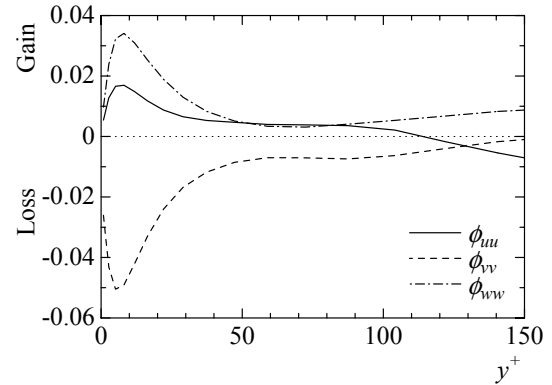


Figure 16: Pressure strain profiles at  $x_{wake} = 2.5\delta$  for  $Re_{\tau_0} = 600$ .

"DNS of turbulent flow in a rod-roughened channel", *Int. J. Heat and Fluid Flow*, Vol.25, pp. 373-383.

Chen, Y. T., Nie, J. H., Armaly, B. F. and Hsieh, H. T., 2006, "Turbulent separated convection flow adjacent to backward-facing step - effects of step height", *Int. J. Heat and Mass Transfer*, Vol.49, pp. 3670-3680.

Comte, P., Lesieur, M. and Lamballais, E., 1992, "Large- and small- scale stirring of vorticity and a passive scalar in a 3-D temporal mixing layer", *Phys. Fluids*, Vol.12, pp. 2761-2778.

Fadlum, E. A., Verzicco, R., Orlandi, P. and Mohd-Yusof, J., 2000, "Combined Immersed-Boundary Finite-Difference Methods for Three-Dimensional Complex Flow Simulations", *J. Comput. Phys.*, Vol.161, pp. 35-60.

Fearn, R. M., Mullin, T. and Cliffe, K. A., 1990, "Non-linear flow phenomena in a symmetric sudden expansion", *J. Fluids Mech.*, Vol.211, pp. 595-608.

Le, H., Moin, P. and Kim, J., 1997, "Direct numerical simulation of turbulent flow over a backward-facing step", *J. Fluids Mech.*, Vol.330, pp. 349-374.

Leonardi, S., Orlandi, P., Smalley, R. J., Djenidi, L. and Antonia, R. A., 2003, "Direct numerical simulation of turbulent channel flow with transverse square bars on one wall", *J. Fluids Mech.*, Vol.491, pp. 229-238.

Lesieur, M., "Turbulence in Fluids", Kluwer Academic Publishers, p. 438.

Nagano, Y., Hattori, H. and Houra, T., 2004, "DNS of velocity and thermal fields in turbulent channel flow with transverse-rib roughness", *Int. J. Heat and Fluid Flow*, Vol.25, pp. 393-403.

Neto, A. S., Grand, D., Metais, O. and Lesieur, M., 1993, "A numerical investigation of the coherent vortices in turbulence behind a backward-facing step", *J. Fluids Mech.*, Vol.256, pp. 1-25.

Rogers, M. M. and Moser, R. D., 1993, "Direct simulation of a self-similar turbulent mixing layer", *Phys. Fluids*, Vol.6, pp. 903-923.